ADVANCED ENERGY MATERIALS
www.advenergymat.de

High Performance and Durable Anode with 10-Fold Reduction of Iridium Loading for Proton Exchange Membrane Water Electrolysis

Jorge Torrero, Tobias Morawietz, Daniel García Sanchez, Dmitry Galyamin, Maria Retuerto, Vlad Martin-Diaconescu, Sergio Rojas, José Antonio Alonso, Aldo Saul Gago, and Kaspar Andreas Friedrich*

Proton exchange membrane water electrolysis (PEMWE) technology is especially advantageous for green H_2 production as a clean energy vector. During the water electrolysis process, the oxygen evolution reaction (OER) requires a large amount of iridium (2-3 mg_{Ir} cm^{-2}) as catalyst. This material is scarce and expensive, representing a major bottleneck for large-scale deployment of electrolyzers. This work develops an anode with 10-fold reduction of Ir loading (0.2 mg_{Ir} cm^{-2}) compared to what it is used in commercial PEMWE for more than 1000 h. An advanced catalyst based on an Ir mixed oxide (Sr_2CaIrO_6) is used for this purpose. Transmission electron microscopy (TEM), X-ray photoelectron spectroscopy (XPS), and X-ray absorption spectroscopy (XAS) analyses show that the unconventional structure of the reconstructed catalyst can contribute to the reduction of Ir in the catalyst layer. The reconfiguration of the ionomer in the catalyst layer is also observed by scanning electron microscopy (SEM) and atomic force microscopy (AFM), results in almost the full coverage of the catalytic layer with ionomer. The results presented herein demonstrate that it is possible to achieve high performance and stability in PEMWE with low Ir loading in the anode without showing significant degradation.

1. Introduction

The reduction of greenhouse gas emissions is one of the pressing challenges for society. Fast deployment of renewable power is necessary to mitigate climate change. Therefore, renewable power is the top priority of the sustainable development goals set by the European Union.[1] Energy storage solutions are required to accommodate the intermittent nature of most renewable energy sources, not only to cover longer-term outages but also to accumulate the surplus of renewable energy. Among those, the so-called green hydrogen, i.e., the hydrogen produced from water electrolysis using renewable energy,[2] is expected to facilitate the transition towards a decarbonized society. This is because green hydrogen can enable to decarbonize sectors with hard to abate emissions such as transport, chemical, and steel

J. Torrero, T. Morawietz, D. García Sanchez, A. S. Gago, K. A. Friedrich
Institute of Engineering Thermodynamics/Electrochemical Energy Technology
German Aerospace Center (DLR)
Pfaffenwaldring 38–40, 70569 Stuttgart, Germany
E-mail: aldo.gago@dlr.de

T. Morawietz
Faculty of Science, Energy and Building Services
Esslingen University of Applied Sciences
Kanalstraße 33, 73728 Esslingen am Neckar, Germany

D. Galyamin, M. Retuerto, S. Rojas
Grupo de Energía y Química Sostenibles
Instituto de Catálisis y Petroleoquímica
CSIC
C/Marie Curie 2, Madrid 28049, Spain

V. Martin-Diaconescu
CELLS – ALBA Synchrotron Radiation Facility
Carrer de la Llum 2–26, Cerdanyola del Vallès 08290, Spain

J. A. Alonso
Instituto de Ciencia de Materiales de Madrid
CSIC
C/Sor Juana Inés de la Cruz 3, Madrid 28049, Spain

The ORCID identification number(s) for the author(s) of this article can be found under https://doi.org/10.1002/aenm.202204169

DOI: 10.1002/aenm.202204169

industry either via Power-to-Liquids (PtL) or Power-to-Gas (PtG) and Power-to-Hydrogen technologies.

A large-scale production of hydrogen by water electrolysis offers the possibility to store electrical energy from fluctuating renewable sources. The production of hydrogen through electrolysis can be used as a method of sustainability through renewable energies. However, currently only 1% of hydrogen demand is produced by water electrolysis.[3] The hydrogen produced from water electrolysis through the use of electricity produced by renewable energies is coined as green hydrogen.[2] The proposal of the European Union goes through the use of green hydrogen to mitigate CO_2 emissions by 2050.[4] For the production of green hydrogen on a large scale and on short time scale, two technologies are promising: proton exchange membrane water electrolysis (PEMWE) and alkaline water electrolysis (AWE).[5]

The PEMWE technology has several advantages: hydrogen can be produced at high pressure and purity, it shows a rapid response and a wide dynamic operation range within an easy-to-maintain compact design and a simple auxiliary system.[6] However, PEMWE technology also present certain drawbacks, the most obvious one being its dependence on scare materials such as platinum group metals (PGM) and its high cost. As a consequence, current research efforts are focused on lowering production costs for instance by decreasing PGM-loading and/or finding alternative less-expensive components.[7]

The main components of a PEMWE cell (Figure 1) are the catalyst coated membrane (CCM), the porous transport layers (PTLs),[8] and the bipolar plates (BPPs).[9] The CCM consists of iridium and ruthenium oxides (IrO_x–RuO_y) as the anode and carbon supported platinum nanoparticles supported on carbon (Pt/C) as the cathode.

During the electrolysis of water two reactions take place: hydrogen (H_2) is formed at the cathode and oxygen (O_2) is produced at the anode.[10] Due to its sluggish kinetics, the production of O_2, known as the oxygen evolution reaction (OER) is the limiting process of water electrolysis. OER catalysts are mainly based on Ru-oxide or Ir-oxide. Although Ru-oxide initially shows higher OER activity,[11] it tends to deactivate and corrode very fast, preventing its use in commercial PEMWEs. Consequently, Ir-oxide is the only catalyst endowed with sufficient OER activity and durability to be used in an actual PEMWE environment.[12–14] State-of-the-art PEMWE electrolyzers use large amounts of Ir-based catalyst at the anode are apparently needed to conduct the reaction at high current densities at low overpotentials.[15] Commercial membrane electrode assemblies (MEAs) for PEMWE have Ir loadings between 2 and 3 mg_{Ir} cm^{-2}.[16] However, the price of Ir is extremely high and volatile, thus being a major contributor to the high cost of PEMWEs.[17] More importantly, the scarcity and ill-distribution of precious metals such as Ir and Pt on Earth, will become a concern when PEMWE installation capacities spread to the GW scale.[18] A drastic reduction in the amount of the Ir used in the anode of PEMWEs is therefore a priority for researchers in the field.[14,19,20]

The OER activity of crystalline Ir-based oxides such as rutile, and of iridium-mixed oxides, such as pyrochlores, perovskites, and hollandites is strongly linked with their crystal structure.[21] The proper design of Ir-mixed oxides may allow to reduce the total amount of Ir in the catalysts while showing OER activity comparable to that of Ir or Ir-oxides.[13,22,23] It is well-accepted that Ir mixed oxides can lose catalytic activity due to oxidation, dissolution, and surface reconstruction under harsh conditions, especially in acidic and oxidative environments.[24] With the assumption of proportional activity contribution a 10-fold reduction of the Ir loading at the anode should not lead to an overpotential larger than 50 mV. Only singular Ir-based catalyst with exceptional OER can be preselected for develop suitable catalyst layer (CL) in PEMWE but at low Ir loadings the intrinsic OER activity of Ir-based catalysts would be not the only limiting factor. Bernt et al.[25,26] have studied the effect of the thickness of the catalytic layer of the anode in the performance offered by PEMWE. For very thin anode electrodes, the performance decreases drastically due to the inhomogeneous noncontiguous character of such thin catalyst layers, resulting in poor anode catalyst utilization. Lower loadings would require the addition of electrically conductive materials that are stable at the high anode potentials of the PEMWE[27] or need modifying other cell components (such as PTLs). The intrinsic OER activity of Ir-based catalysts would be enough if the iridium density in the electrode could be reduced, so that electrodes with low Ir loadings would increase in thickness.[25] Therefore, not only the catalyst activity for the OER is important, but also its morphology/structure to achieve thin anodes with promising performance.

Recently, Retuerto et al. have synthesized different Ir double perovskites (Sr_2CaIrO_6) with the Ir atoms in a high oxidation state ($Ir^{6+/5+}$)[28] and their catalytic activity was extensively investigated. Specifically, a Ca-based double perovskite (Sr_2CaIrO_6) has showed the highest OER activity similar to those of Ir or Ir oxides-based catalysts while being stable for the OER in half cell measurements.[29] In this work, we developed an anode with Sr_2CaIrO_6 catalyst that has only 0.2 mg_{Ir} cm^{-2}, that is 10 times lower compared to what it is used in the anodes of commercial PEMWE, showing remarkable performance and stability. The morphology/structure of the developed anode and Sr_2CaIrO_6 catalyst, before and after operation in PEMWE, were extensively characterized by X-ray diffraction (XRD, high-resolution transmission electron microscopy (HRTEM), scanning electron microscopy (SEM), atomic force microscopy (AFM), X-ray photoelectron spectroscopy (XPS), and X-ray absorption near edge structure (XANES). Thus, this work provides as well, a comprehensive study on the origins of the high OER activity and stability of PEMWE anodes with significant reduction of Ir and the associated degradation mechanisms (**Figure 1**).

2. Results and Discussion

2.1. Crystal Structure of Sr_2CaIrO_6

Sr_2CaIrO_6 is a mixed oxide with double perovskite structure ($A_2BB'O_6$). Ca^{2+} and Ir^{6+} cations are located at the octahedra B positions of the structure and Sr^{2+} at the A positions, in a coordination close to 8. The compound presents cationic ordering between Ca and Ir cations over two different BO_6 and $B'O_6$, with a monoclinic crystal structure, space group $P2_1/n$. The initial material was characterized before using several techniques, such as X ray and neutron powder diffraction.[30,29]

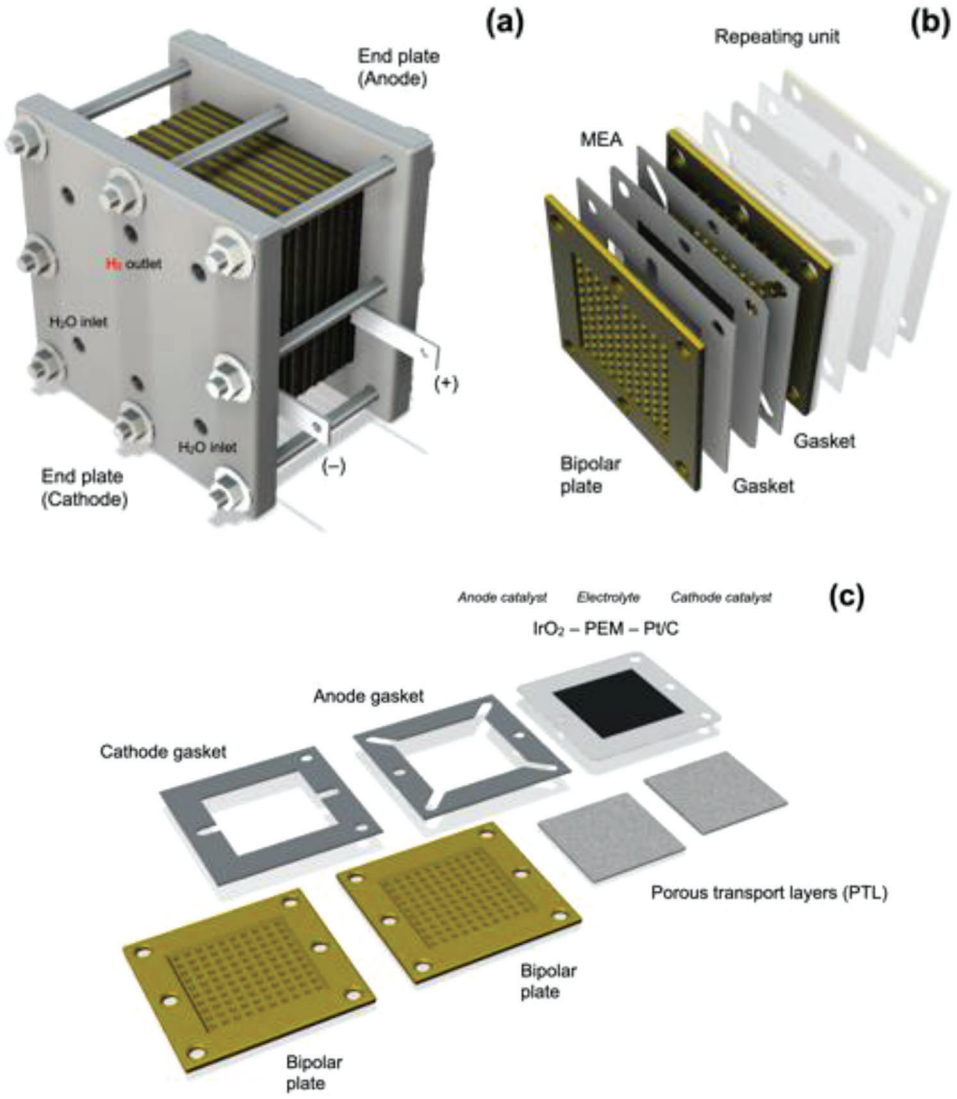

Figure 1. Schematic drawings a) commercial proton exchange membrane water electrolysis (PEMWE) stack; b) repeating unit cell; and c) cell components.

2.2. Electrochemical Performance and Durability for Sr_2CaIrO_6 in PEMWE

Before stating the development of the PEMWE anode with 0.2 mg_{Ir} cm^{-2} of Sr_2CaIrO_6, catalyst, the OER activity was confirmed in a rotating disk electrode (RDE) configuration by recording cyclic voltammograms between 1.1 and 1.7 V_{RHE} at 10 mVs^{-1} and a rotation rate of 1600 rpm in O_2-saturated 0.1 M $HClO_4$. Figure S1 (Supporting Information) shows that Sr_2CaIrO_6 reaches 1.48 V to achieve 10 mA cm^{-2}, a value typically used to benchmark the OER activity of catalysts.[31] This value is among the highest ones reported in the literature comparable to $SrTi_{0.67}Ir_{0.33}O_3$,[23] 6H-$SrIrO_3$,[32] $SrZrO_3$:$SrIrO_3$ (Zr:Ir 1:2),[33] and 3R-IrO_2,[34] oxides; and Ir NSs,[35] $Ir_{44}Pd_{10}$,[36] and IrRu@WO_3.[37] However, high OER activities in RDE do not always translate into real application in PEMWE. This is particularly relevant for the assessment of catalyst durability, and in general OER catalyst lifetimes recorded in RDE are three to four orders of magnitude lower than those measured in a PEMWE.[31] However, such OER activities are not always maintained because many Ir-based oxides undergo dissolution and surface modification. Zhang et al. observed that the OER activities of Ir-based perovskites are generally dominated by the oxides formed on the catalyst surface.[24]

Considering the activities shown by the catalyst Sr_2CaIrO_6 for the OER and to demonstrate its usefulness with low Ir loadings, the catalysts has been integrated as an anode in a PEMWE with low loadings. The stability at low loadings is one of the mayor issues in the reduction of Ir loadings PEMWE. State-of-the-art commercial PEMWEs use an Ir loading of 2–3 mg_{Ir} cm^{-2} in the anode.[9] According a previous report,[38] the large-scale production of PEMWEs demands a drastic reduction of the Ir loading to 0.25–0.4 mg_{Ir} cm^{-2},[39] or more precisely, to loadings that are low enough to reach iridium-specific power densities of

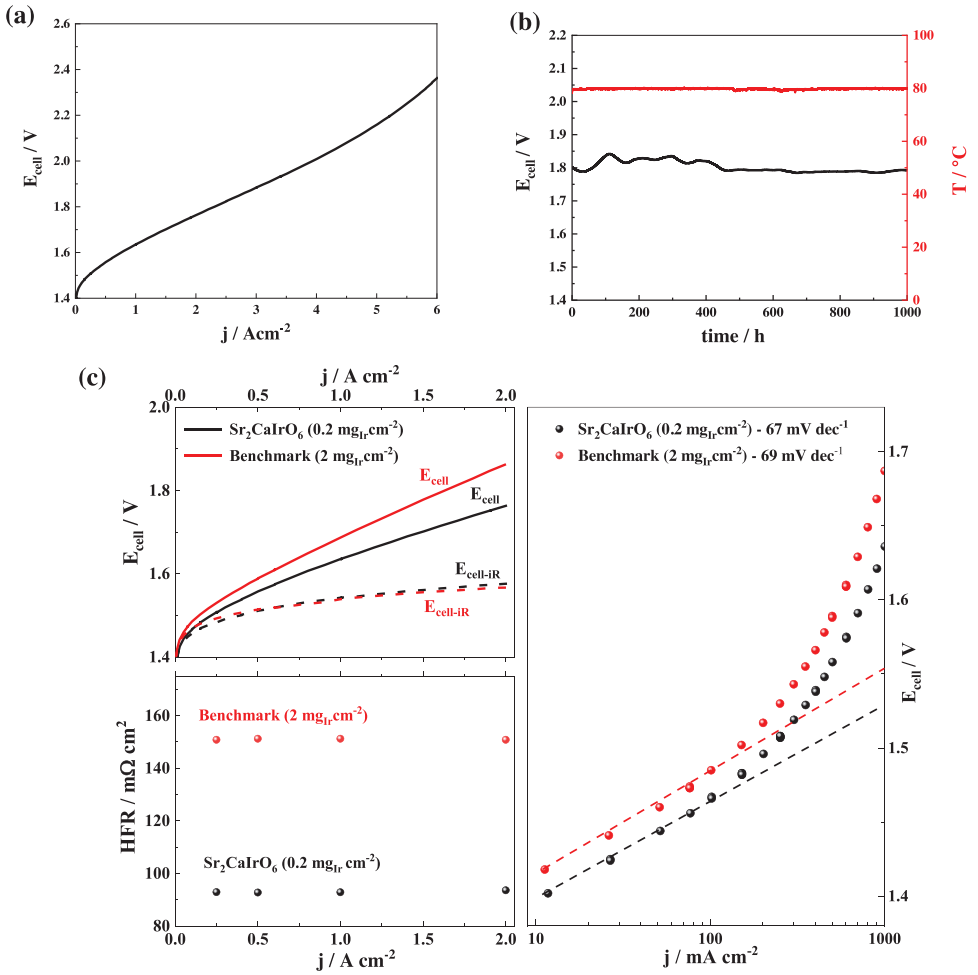

Figure 2. Proton exchange membrane water electrolysis (PEMWE) measurements with the Sr_2CaIrO_6 anode (0.2 mg_{Ir} cm^{-2}) and Pt/C (commercial) cathode (0.4 mg_{Pt} cm^{-2}) carried out at 80 °C and ambient pressure: a) Cell potential (E_{cell}) with respect to the current density (j) recorded galvanostatically up to 6 A cm^{-2} (overload) according to the JRC EU-harmonized, b) E_{cell} and cell temperature (T_{cell}) evolution over time (1000 h) at a constant 2 A cm^{-2} (nominal load). c) Current voltages curves and high frequency resistance (HFR) values versus current density obtained by electrochemical impedance spectroscopy (left panel) and Tafel slopes between 10 and 100 mA cm^{-2} of the iR-free cell voltage (right panel) carried out at 80 °C and ambient pressure for comparation between Sr_2CaIrO_6 (0.2 mg_{Ir} cm^{-2}) and benchmark iridium oxide anode (2 mg_{Ir} cm^{-2}).

≈0.01 g_{Ir} kW^{-1} at 70% LHV.[25] According to the RDE measurement the Sr_2CaIrO_6 fulfils this criteria so it qualifies as candidate to achieve a 10-fold reduction on Ir loading and develop an anode with 0.2 mg_{Ir} cm^{-2} without compromising neither activity nor durability.

For catalyst performance studies, CCMs were prepared as explained in Section 4 (Experimental Section) and they are composed by Sr_2CaIrO_6 to a final Ir loading of 0.2 mg_{Ir} cm^{-2} in the anode and Pt/C catalyst in the cathode. CCMs were produced through spray deposition coating on Nafion 212 membrane (50 µm). As PTL, Ti porous sintered layer (PSL) on Ti mesh compound produced by diffusion bonding coated with Pt was used (PSL/mesh-PTL).[40] Ti plates were used as BPP. Water electrolysis testing was conducted in a 4 cm^2 single cell with polarization curves and durability test recorded at 80 °C and ambient pressure. Ideally, PEMWE cells should transiently operate at much higher current densities of 6 A cm^{-2} instead of the state-of-art of 2 A cm^{-2},[41] while keeping efficiencies above 70%.

Figure 2a shows a polarization curve recorded up to 6 A cm^{-2} reaching an E_{cell} of 2.36 V while not exceeding 2.5 V. Cell operation at this high potential is economically not attractive, so it is more appropriate to report E_{cell} at nominal current density of 2 A cm^{-2}. PEMWE reported in our work reaches an E_{cell} of 1.78 V at 2 A cm^{-2}. This performance is comparable to the most recent reports of PEMWE with low Ir loaded anodes.[25,42–44] For further comparison, PEMWE commercial electrolyzers, such as those from Hydrogenics,[16] Siemens,[45] and Proton Onsite[46] achieve about 2.2 V at 2 Acm^{-2}. In addition to demonstrate a good initial performance, the novel catalyst must prove to be stable over extended operating time under PEMWE conditions. Commercial PEMWEs have a half-life of at least 10 000 h.[6] Möckl et al.[18] have shown that a few hundred hours can provide an initial indication of catalyst's performance. Furthermore, we have tested durability by recording 1000 h at constant current density of 2 A cm^{-2} at 80 °C and ambient pressure to evaluate the stability of the catalyst. As shown in Figure 2b, the PEMWE using Sr_2CaIrO_6

as the anode shows a stable response, with no significant E_{cell} drop even after 1000 h of continuous operation, offering practically the same E_{cell} as at the beginning of the operation, with just a 10-mV increase. This value also obtained by the polarization curve carried out at begging of test and end of the test after 1000 h (see Figure S2, Supporting Information). The response of the PEMWE with the Sr_2CaIrO_6 anode is similar than that obtained in the long-term tests reported in the literature, recording similar degradation rates than other Ir-based catalysts.[26] As shown in Figure 2a faster degradation takes place during the early stages of the durability test. Then, the response stabilizes offering an almost constant E_{cell}, in good agreement with the observations by Möckl et al.[18] Other works like Rakousky's et al.[47] show that while the E_{cell} remains constant there is a decrease in ohmic resistance.

To compare the results obtained with Sr_2CaIrO_6 with a reference that has similar characteristics than commercial CCMs,[9] a CCM prepared with benchmark IrO_2 as anode (2 mg_{Ir} cm^{-2}) and Nafion 115 (127 μm), which is what is used in commercial CCMs, was tested under the same conditions using identical cell hardware. Since different membranes were used (Nafion 212, 50 μm thick and Nafion 115, 125 μm thick see Experimental Section), the high-frequency resistance (HFR) values for both configurations have been measured and used for a valid comparison of the catalyst effect. Figure 2c shows the polarization curves up to 2 A cm^{-2} (upper panel) and HFR (bottom panel) obtained for the PEMWE. Electrochemical impedance spectroscopy (EIS) was performed at different current densities and for the Nyquist plots an equivalent circuit consisting in three elements was used for modeling the results (see Section S1, Figure S3, Supporting Information). The HFR values are determined from the intercept with the real axis taken from the Nyquist diagrams obtained. As expected, the HFRs for the PEMWE with low Ir loading (0.2 mg_{Ir} cm^{-2}) show lower values (≈30%) than those for higher loading (2 mg_{Ir} cm^{-2}) due to the different thicknesses of the CCMs. However, after *i*R-correction the polarization curves of both configurations are almost identical, see Figure 2c, showing only a minor deviation of 1% E_{cell} at 2 A cm^{-2} despite the high differences in the Ir loading of both CCMs. Tafel slopes have been determined to better understand the behavior of the low current density region. A linear fitting in the Tafel plot in Figure 2c (right panel) has been made between 10 and 100 mA cm^{-2}. The anode with Sr_2CaIrO_6 has a Tafel slope of 67 $mVdec^{-1}$, which is similar to the benchmark catalyst of 69 $mVdec^{-1}$, indicating that the OER kinetics of novel anode with Sr_2CaIrO_6 are similar to IrO_2 but with a reduction of Ir loading by a factor of 10. With these results, Sr_2CaIrO_6 shows to be an active and stable alternative to other Ir-based catalysts such as those studied by Chatterjee et al.[44] or Möckl et al.[18] with similar iridium loads in the PEMWE anodes. The achievement of the type of catalysts shown in this work can be a game changer for this technology.

2.3. Characterization for Sr_2CaIrO_6 Before and After Operation During 1000 h

It is well accepted that the activity presented by Ir-based catalysts is closely linked to their structure, or more likely to their surface structure and composition.

To understand the evolution of the catalyst composition, structure, and morphology after 1000 h operation, an extensive ex situ characterization has been performed. The evolution of the catalysts and its surface during the reaction was assessed by characterizing the operated anode (after 1000 h) which is named Sr_2CaIrO_6-end of test (EoT) anode. The structure of the EoT anode has been compared with a nonoperated anode, or pristine anode, i.e., the catalyst sprayed on the Nafion 212 membrane (from the water/isopropanol/Nafion ink) but previous to OER, that we refer as Sr_2CaIrO_6-beginning of test (BoT). Also, an activated anode or Sr_2CaIrO_6-short time test (SoT) anode which is an anode after short operation time, has been characterized.

The BoT and EoT CCMs have been analyzed by powder XRD. The XRD are shown in **Figure 3**a. As synthesized the Sr_2CaIrO_6 powder has a double perovskite structure.[29] However, since we recorded X-ray diffraction patterns of the CCM, phase from the anode and the cathode together with the membrane are observed. The diffractogram for the BoT displays mainly the reflections of Pt/C from the cathode. A set of weak reflections at ≈31°, 55° and 74° is also observed. These diffraction lines correspond to the most intense reflections of the perovskite. However, after the test of 1000 h, the diffractogram for the EoT CCM fails to show reflections from the perovskite phase. However, diffraction features from the Pt fcc phase (from Pt/C cathode) along with faint reflections probably arising from the nafion are observed.

The structure of the catalysts of both anodes (BoT and EoT) was studied by transmission electron microscopy (TEM). For this study, particles were detached from the CCM by scraping. Figure 3b shows that the BoT catalyst is composed of particles of around 500–1000 nm. The XRD analyses indicate that the large crystalline particles display the perovskite phase. However, most of these particles fail to display the original Sr_2CaIrO_6 composition as they do contain much lower content of Ca^{2+} and Sr^{2+} than the initial perovskite (see SEM Section). The HRTEM of the periphery of one of the large particles (see Figure 3b) shows the presence of Ir-rich nanoparticles at the surface of the perovskite. It means that many of these non-noble metals have been dissolved by just immersing the catalyst in the ink suspension.

After 1000 h of operation, at EoT anode, the morphology and composition of the catalyst changes further (Figure 3b–d). The catalyst is composed by large particles, but a closer inspection of the micrographs reveals these are not bulk and dense particles, but they present a sponge-like morphology, with voids across the entire particles Figure 3. Energy dispersive X-ray analysis (EDS) performed after test showed that the particles are composed only by Ir and O as Ca and Sr continue to dissolve during the reaction. Figure 3c shows a close image of one region of the particles. They are conformed by amorphous nanoregions (of around 2 nm) which are most likely Ir–O–H species. The formation of IrOOH species on Sr_2CaIrO_6 after RDE cycling has been previously observed,[29] as well as the formation of this type of open structures. Previous studies about the evolution of Ir mixed oxides during the OER report the formation of IrO_x and/or IrOOH at the surface of the original mixed oxide, in some cases the original mixed oxide being fully transformed into IrO_2 and/or $IrOOH_x$.[24,28,48,49] However, the reconstruction of the Sr_2CaIrO_6 particles after depostion on the CCM is different to that reported in previous works. First of all, the

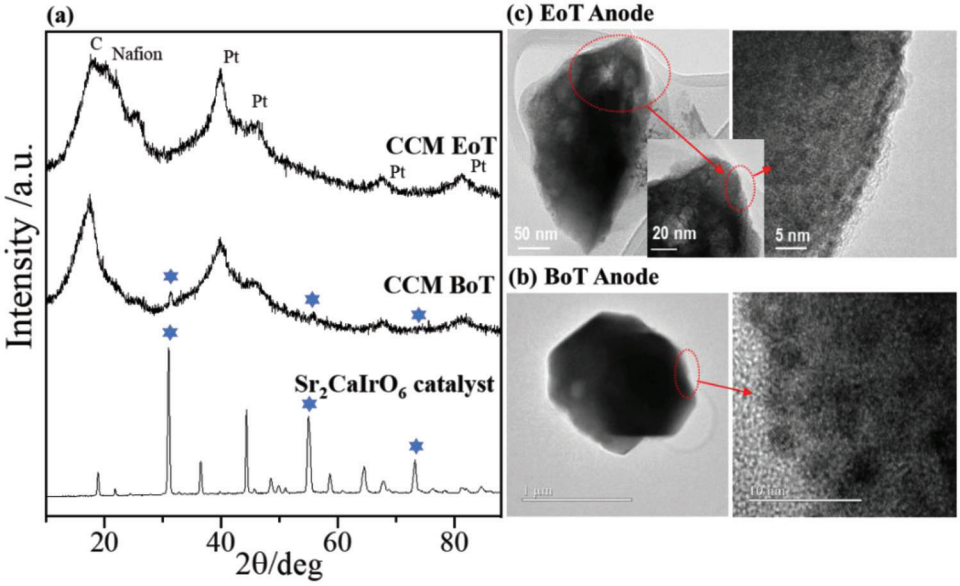

Figure 3. a) X-ray diffraction patterns of the Sr_2CaIrO_6 catalyst as synthetized, the catalyst coated membrane (CCM) BoT and the CCM EoT. b) Transmission electron microscopy (TEM) and high-resolution transmission electron microscopy (HRTEM) micrographs of the BoT anode.) TEM and HRTEM micrographs of the EoT anode. Note that the nanoparticles appearing in Figure 3c are Pt/C contamination from the cathode, since the particles have been removed directly from the CCM.

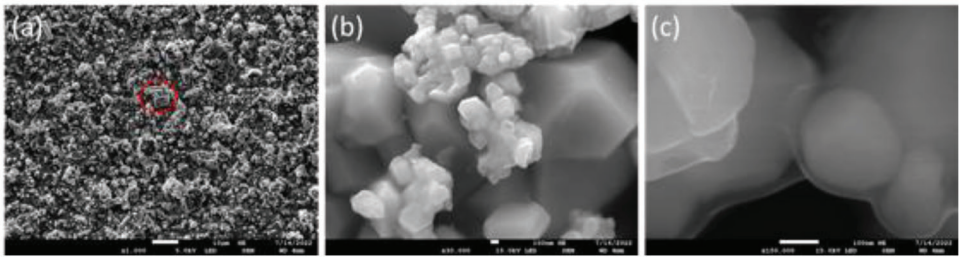

Figure 4. Scanning electron microscopy (SEM) images of BoT anode with a) 1.000×, b) 30.000×, and c) 150.000× magnification; the white scale bar represents on a) 10 µm; b) and c) 100 nm.

sponge-like morphology, with an open structure, is unique to Sr_2CaIrO_6. We believe that this structure is formed due to the fast leaching of Ca, that produces a strong reconstruction on the surface. In this reconstructed surface, the Ir regions are not ordered in small individual IrO_x/IrOOH nanoparticles, as it is usually observed,[48] but in a very amorphous surface layer of Ir–O–H (Figure 3d).

Complementary, SEM measurements were carried out for both BoT and EoT anodes, allowing a broader vision of the catalyst structure on the CCM. For the sake of completeness SEM measurements of the cathode can be found in Section S2, Figures S3 and S4 (Supporting Information).

The structure of the anode layer with Sr_2CaIrO_6 shows three different size characteristics. Large crystals with an extension in the micrometer range are visible. The largest crystals extend up to 10 micrometers marked in **Figure 4**a. In addition, there are crystals with a size between ≈100 and 400 nm (see histogram of all crystal sizes in Figure S9e, Supporting Information) that have formed agglomerates and are typically deposited on the larger crystals (Figure 4b) comparable to the results measured with TEM. The ionomer layer covering the particles can be observed at the edge which is shown in Figure 4c.

From the secondary electron SEM images in **Figure 5**a–f for BoT, EoT, and SoT, respectively, one can see that on anode side the membrane is not completely covered with the catalyst, due to the high density and large particle size of the Sr_2CaIrO_6. This can be seen in comparison later in the secondary electron SEM images in Figure 5a–f for BoT, EoT, and SoT, respectively. The structure of the catalyst and the interaction with the ionomer was studied in detail by SEM (Figure 5) and AFM (**Figures 6** and **7**). Like described above, it can be seen in the SEM measurements that the Sr_2CaIrO_6 catalyst are micrometer sized crystals but smaller particles around 100–400 nm and below in size can also be seen. The smaller sized crystals are shown in the SEM micrographs in Figure 5a,d for the BoT anode. The SEM measurement for the SoT in Figure 5b,e also confirms that the morphology was not affected by the short-time PEMWE operation.

The EoT anode consists mainly of the large, structured crystals but lacks the presence of smaller crystals. The energy dispersive spectroscopy (EDX) measurement in Figure 5g–i of fluorine

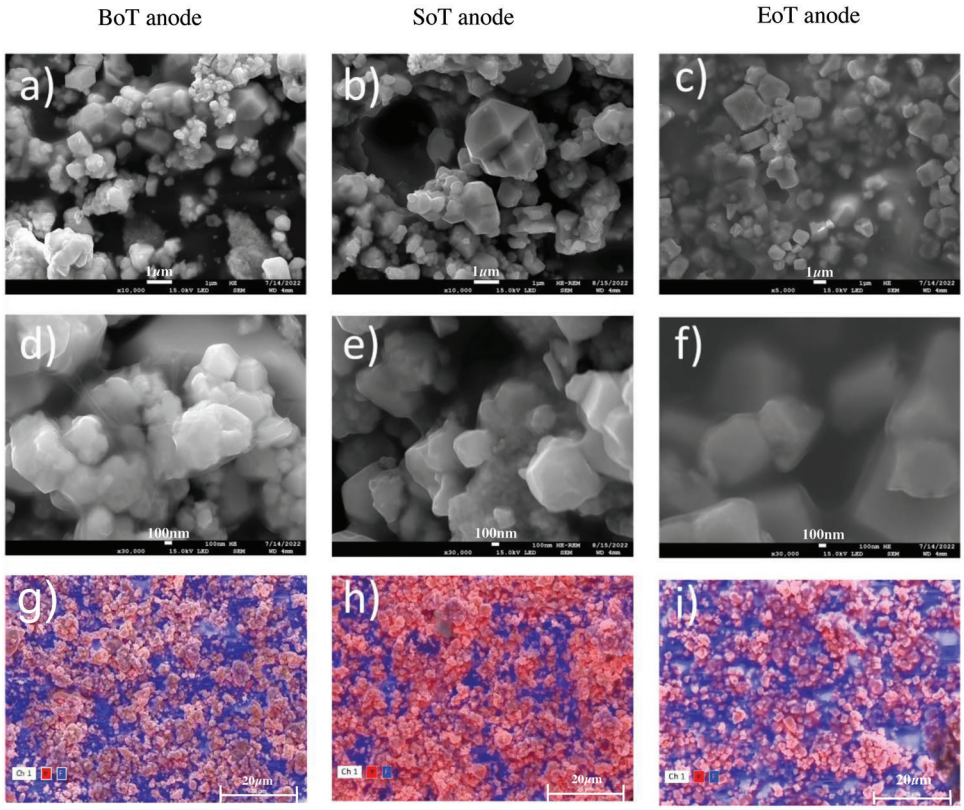

Figure 5. Before and after stability test characterization (scanning electron microscopy (SEM)). a) BoT anode 10.000×, b) SoT anode 10.000×, c) EoT anode 5.000×; White scale-bar represents 1 µm on (a–c). d) BoT anode 30.000×, e) SoT anode 30.000×, f) EoT anode 30.000×; White scale-bar represents 100 nm on (d–f). g–i) Quantitative energy dispersive spectroscopy (EDX) mappings with a scale-bar of 20 µm (iridium = red, fluorine = blue): g) BoT anode, h) SoT anode, i) EoT anode.

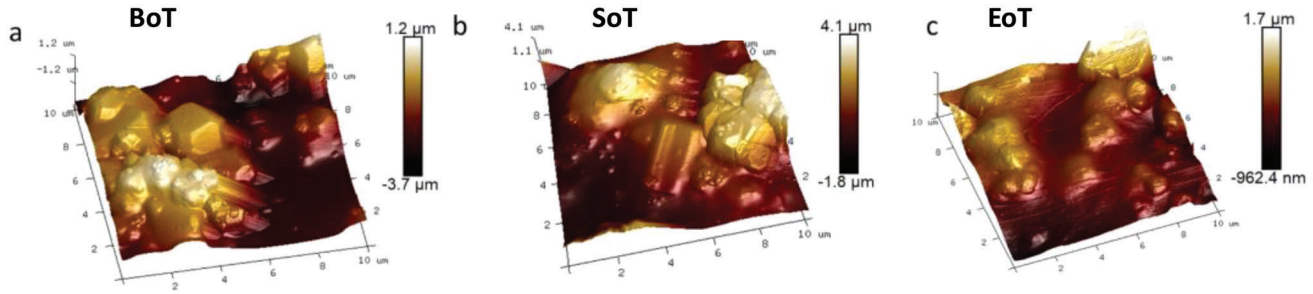

Figure 6. Atomic force microscopy (AFM) height measurements with an area of 10 × 10 µm^2 for a) BoT, b) SoT, and c) EoT.

and iridium underlines this statement. EDX measurements revealed the presence of Sr and Ca on BoT and SoT catalyst, but their content decreases after operation, like it was observed with TEM. Still, after operation for 1000 h at a large-scale Sr and Ca could be found in a lower amount when compared to BoT anode. Bar charts for elemental SEM/EDX analysis for BoT, EoT, and SoT can be found in Figure S14 (Supporting Information). This structure of large catalyst particles can be advantageous for the performance of the catalyst layer due to low or null tortuosity. The rate determining step for the electrolyte flux at this catalyst layer structure is then the connection to the other components like the PTL. The thickness of the catalyst layer is 1–3 µm depending on the number of stacked large crystals that are kept together by the ionomer. The thickness was measured with SEM using ion-cut samples of the CCMs. It is noted that the membrane was damaged by the cut with argon ions, but the focus here is on the catalytic layer. Several SEM secondary electron measurements and EDX mapping images at different resolution of the ion-cuts samples can be found in Figures S5–S7 (Supporting Information).

To study the ionomer coverage, conductive and nanomechanical AFM was performed on the surface of the three anodes at different operation times, that is BoT, SoT, and EoT. In addition to the measurements of the nanoelectrical and nanomechanical properties measurements with high resolution AFM tips reveal the topography of the catalyst layer as 3D images, see Figure 6. Height profiles of these structures can be found in Figure S15

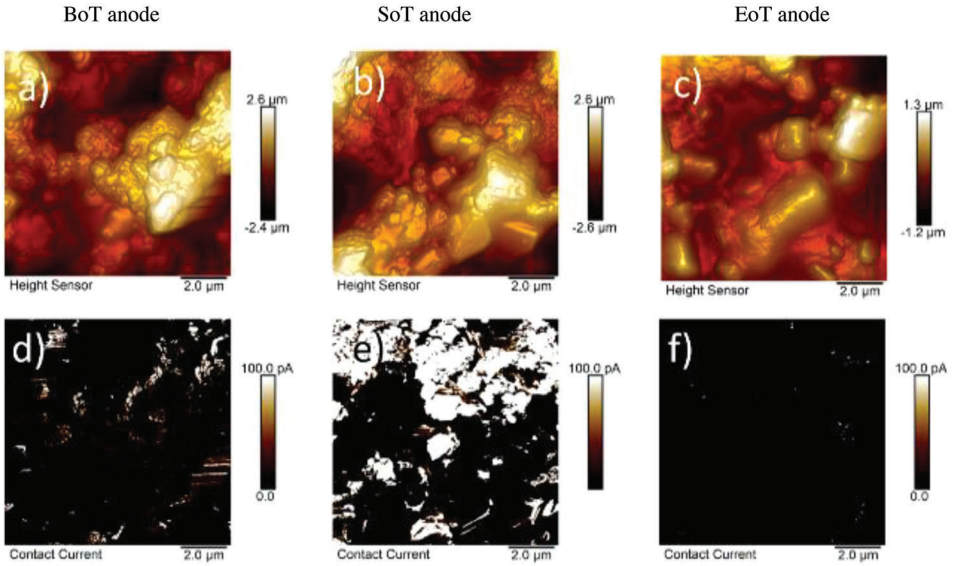

Figure 7. Atomic force microscopy (AFM) height measurements of anodes a) BoT, b) SoT, c) EoT and the corresponding AFM electronic conductivity measurements d) BoT, e) SoT and f) EoT.

(Supporting Information). The smoother surface of the EoT sample due to a higher ionomer coverage is obvious from these measurements.

With nanoelectrical and nanomechanical AFM measurements in PeakForce-TUNA mode (Figure 7) the ionomer seems to cover a large part fraction of the particles, which can be clearly seen in the measurements of the electronic current. For this purpose, a voltage is applied between the catalytic layer and the AFM tip coated with PtIr, and thus the electron flux at the areas is not covered with ionomer is measured. The BoT anode shows a low electronic conductivity and therefore a high ionomer coverage. Remarkably, the conductive area is only 2–3% of the measured area of 10 µm. The ionomer can be further distinguished in addition from the catalyst by higher deformation and adhesion as well as lower stiffness (shown in Supporting Information). The coverage with ionomer on the surface is approx. 49% from measuring the deformation. From this result, a low interconnection between the single crystals can be assumed, as the back contact of the electronic current was based on the side of the sample. Interestingly, this does not prevent the good electrochemical performance reported in the specific Section 2.2.

SEM in Figure 5d shows how the ionomer is located between the particles, acting as binder and ensuring the ionic conductivity. In the Supporting Information, representative SEM images with a higher resolution are shown in which the ionomer is clearly visible (Figure S9, Supporting Information). A high amount of ionomer coverage can be assumed for the BoT anode by the AFM measurements. This situation clearly changes after a short activation, as the conductive area of the SoT anode measured with AFM increases by a factor of 10 (Figure 7). The nanomechanical properties, like the deformation information derived from AFM force-distance curves (Figure S17, Supporting Information) confirm this observation. The ionomer distribution can also be imaged with SEM. Thus fluorine EDX mapping after activation revealed a reduced ionomer coverage which is visible in the SEM measurements as well as in the EDX mappings, which show less fluorine coverage. This result is clearly observed from the false color mappings for the fluorine content in Figure S11 (Supporting Information). The area of low adhesion and low deformation (uncovered catalyst particles) measured with AFM increases after activation, as the fluorine content decreases at the surface of the catalyst layer measured with EDX mapping, shown in blue color (Figure 5g–i and Figure S11, Supporting Information, concentration mapping). This effect is in good agreement with the electrochemical measurements, where the OER activity improves after the activation process.

A good combination of ionic and electronic conductivity with catalytic activity is essential for high performance. Optimal electrical and structural properties for the catalyst layer have not been determined so far, and more research is required. In this work, it can be shown that not necessarily a good contact between the different particles is crucial for high performance, but the interaction between the ionic and the electronic conductivity as well as a good accessibility of the catalyst is essential. A good electrical back-contact can be achieved by an optimized PTL. An ionomer layer of about 10–30 nm can be assumed, with the thickness typically having some distribution, as shown for fuel cells by Morawietz et al.[50] and Lopez-Haro et al.[51] in the case of fuel cells (PEMFC). The imaging of the ionomer with the SEM in the Pt/C catalyst layer in PEMFC is difficult because the contrast between carbon and ionomer is often insufficient. In the case of PEMWE, the contrast is superior with Ir nanoparticles, which is why the ionomer, at the edge of the particles, can be distinguished from the catalyst in the SEM. An example is shown in Figure S9c,d (Supporting Information); however, the quantification of ionomer coverage is still challenging, as the ionomer on the surface only shows as a blurred image at these areas. However, at the boundaries of the particles, the ionomer can be transmitted and thus the ionomer layer thickness can be measured.

A structural change due to the ion beam cannot be excluded. To obtain complementary and supplementary measurements of the properties, AFM measurements were performed in addi-

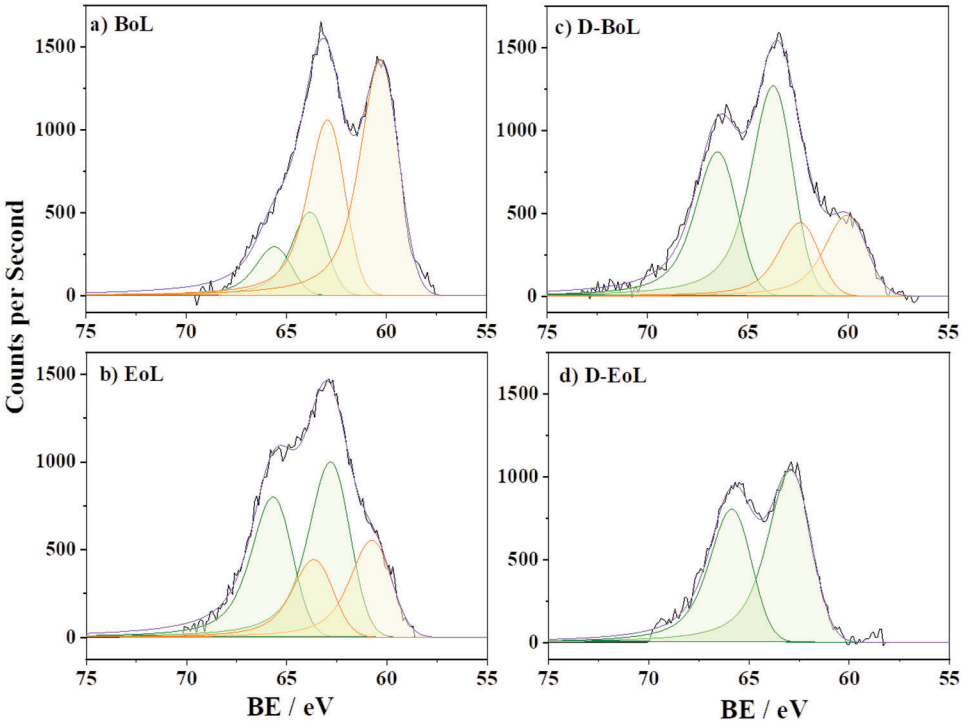

Figure 8. Ir 4f core-level region of the BoT (a) and end of test (EoT) (b) anodes. The prefix D-indicates the analysis of the inner layers of the catalyst at the BoT (c) and EoT (d) anodes.

tion to SEM measurements. The advantage of AFM in this context is the measurement carried out without vacuum and without the influence of an electron beam. At EoT anode, however, an opposite effect can be seen for the ionomer coverage than what was the case after activation. The particles that are almost completely enveloped by ionomer remain stable in the catalytic layer: It seems like crystals are inside the membrane either due to softening of the membrane ionomer or a rearrangement of the ionomer from the anode. In the SEM surface images, this effect can be seen in as more blurring of the catalyst layer (Figure 5c) but the AFM images (Figure 7c,f) the result is almost nonexistent electronic conductivity. In addition, a significantly reduced coverage of the membrane with catalyst can be seen in the EDX measurements (Figure 5i), where a higher area of fluorine is measured. The lower coverage of the membrane surface is also noticeable in the SEM measurements. It can be derived that ionomer covers the surface leading to the low electronic conductivity, similarly to what has been reported by Morawietz et al.[50] The EoT anode has a significantly reduced electronic conductivity, where one can see that almost the entire surface is covered with ionomer. The conductive areas, i.e., the areas not covered with ionomer and connected coherently, are only 0.1% after operation for 1000 h. Despite this large decrease in electronic conductive, the electrochemical activity of the anode remains high, indicating that only the electronic contact to the PTL is relevant and not the in-plane conductivity of the catalyst layer, and not the cross-conductivity between the individual catalyst particles.

Further SEM and AFM measurements on the surface and ion-cut samples are shown in Figures S5 and S6 (Supporting Information). It is assumed, that the crystals, which are larger and coated with ionomer, have a higher stability than uncovered small particles. The disappearance of the smaller crystals after the operation time of 1000 h can also account to Ostwald-ripening.[52–54] The unconventional structure morphology of Sr_2CaIrO_6 contributes to the reduction of Ir in the catalyst layer and demonstrates a new approach that can be expected to lead to further improvements and enables long-term operation without a significant decrease in catalytic activity.

Moreover, the surface nature of the cations and composition of the Sr_2CaIrO_6 anode was analyzed by XPS, see **Figure 8**. The evolution of the surface during the reaction was assessed by comparing the spectra for the fresh sample, i.e., before reaction (BoT), and of the CCM recovered after 1000 h of reaction (EoT). In addition, the compositions of the outmost layer and of an inner layer of the CCM before and after the OER (D-BoT, and D-EoT, respectively) were analyzed to assess the homogeneity of the catalytic layer.

The XPS spectra of all samples reveal the presence of Sr and Ir (along with O and C), but fail to show the presence of Ca (see Section S6, Figure S18, Supporting Information). This result indicates that Ca cations are leached from surface of the catalyst already during ink preparation and/or catalyst deposition on the membrane. In line with previous reports, and in order to account for screening effects, the Ir 4f core-level regions were adjusted using asymmetric peaks, with a spin-orbit splitting of ≈2.98 eV and a peak area ratio of ≈4/3. The Ir 4f core-level spectrum of BoT anode shows two doublets, with the binding energies of the Ir 4f7/2 peaks at ≈60.0 and 63.5 eV, see Figure 4a. After operation, the spectrum of EoT anode also records two doublets, with

the Ir 4f7/2 peaks at ≈60.4 and 62.4 eV, see Figure 4b. The peak at ≈60 eV is typically ascribed to metallic Ir species. However, such an assignment would be counterintuitive for our sample, since Sr_2CaIrO_6 has been synthesized under high O_2 pressure at high temperature, resulting in Ir > 4+ cations.[28] It is known that the actual BE of the Ir signal is related to its local structural environment. For instance, Chen et al.[55] studied the XPS spectrum of monoclinic $SrIrO_3$ (m-$SrIrO_3$), which is a monoclinic distortion of the 6H-hexagonal perovskite, and concluded that the Ir 4f7/2 peak at 60.33 eV should be ascribed to Ir4+ species. In m-SrIrO3, part of the IrO6 (with Ir4+) octahedra are face-shared on Ir_2O_9 dimers. In these dimers, the Ir–Ir distances are relatively short, 2.770(8) Å,[56] a value similar to Ir–Ir distances in metallic Ir[57] and much closer than in most Ir oxides and mixed oxides.[30,58] With this discussion in mind, we ascribed the species at ≈60.33 eV to cationic Ir species, probably Ir4+. Moreover, such an assignment is consistent with the X-ray absorption spectroscopy (XAS) results shown below. A deeper analysis of the XPS spectra shows that only Ir and Sr (along with O) atoms are present at the surface, so it is possible that a phase akin to m-$SrIrO_3$ has been formed at the surface of the catalyst upon Ca dissolution. This view is also consistent with the analysis of the Sr 3d region. In BoT anode, the position of the Sr 3d5/2 core-level at 133.4 eV characterizes Sr cations in mixed oxides such as SrTiO3. Admittedly, this BE is also found for other Sr species, including Sr oxides, hydroxides and/or carbonates.[59] In addition, as observed by XPS not only Ca, but also a fraction of Sr atoms is leached. Thus, the surface atomic Ir/Sr ratio of 0.8 found for BoT anode is closer to the value of 1 expected for SrIrO3 than to the stoichiometric value of Ir/Sr = 0.5 expected for Sr_2CaIrO_6.

The second Ir 4f doublet at higher BE is usually ascribed to the presence of shake-up satellite peaks, which appear at ≈1 eV higher BEs than the main peak. However, the Ir 4f7/2 peak of the second doublet is centered at 63.5 eV, i.e., at higher BEs than those expected for satellite peaks, suggesting that this doublet characterizes Ir cations in high oxidation state, Ir > 4+ as expected for the Ir atoms in Sr_2CaIrO_6. The Ir 4f core-level region of the spectrum of the sample after 1000 OER cycles (EoT anode) also displays two doublets, with the Ir 4f7/2 peaks at 60.3 and 62.4 eV.[60] Contrary to the spectrum BoT, after the OER, the doublet at high BE (62.4 eV) is more intense than the one at low BE (60.3 eV). In addition, the peak at high BE shifts by ≈1 eV to lower energy as compared to the high BE peak (63.5 eV) in the spectrum for BoT, suggesting that Ir > 4+ species have evolved into Ir4+/3+ species. Note that the precise assignment of Ir3+ and Ir4+ species by XPS is not straightforward. In part, this is due to the fact that Ir3+ species may appear at higher BE than Ir4+ ones, at least in pure oxides.[56]

The Sr 3d core-level spectrum for EoT anode shows a peak at 134.3 eV, a value typically reported for strontium carbonates. The surface atomic Ir/Sr ratio increases to 1.25 (0.8 in the fresh sample, see above) indicating a progressive dissolution of Sr during the OER. The analysis of the inner layer of the catalyst layer by XPS reveals the same trends. The spectrum for BoT anode (Figure 8c) shows two doublets, with Ir 4f7/2 peaks at 59.7 and 63. 4 eV. After reaction, a single doublet at 62.5 eV is observed (Figure 8d). In summary, the XPS analysis of the CCMs indicate a surface reconstruction from the initial catalyst Sr_2CaIrO_6, into a mixture of SrIrO3 and Sr_2CaIrO_6 after catalyst deposition on the MEA due to Ca and Sr dissolution, and finally into a mixture of IrO_2/IrOOH species after the OER.

XAS was performed on the BoT and EoT anodes. **Figure 9**a shows the Ir L_3-edge XANES signal of both anodes together with $IrCl_3$ and IrO_2 standard. The white line position of BoT anode (11219.3 eV) is the same as that of IrO_2, indicating that the oxidation state of Ir is close to +4. However, after 1000 h operational cycles a shift of the white line position toward lower energies (11218 eV) is observed for the EoT anode, closer to $IrCl_3$ (11217.7 eV) indicating a reduction of Ir oxidation state and probably also a change in the environment of Ir during the OER. This evolution is consistent with the possible formation of an amorphous phase similar in structure to IrO_2 or $SrIrO_3$ for BoT and followed by a partial reduction of Ir oxidation state during operation, probably resulting in the formation of IrOOH.

Figure 9b depicts the evolution of the Fourier transform (FT) from the Ir L_3-edge extended X-ray absorption fine structure (EXAFS) signals. The first coordination shell around 1.9 Å is attributed to the Ir–O distances. In BoT anode this distance is very similar to Ir–O found in IrO_2, $SrIrO_3$, and Sr_2CaIrO_6.[30,58] However, EoT anode shows a slight increment of the Ir–O bonds indicating more reduced Ir atom, in accordance with the formation of nanoregions of IrOOH, in which the Ir–O distances are close to 2 Å.[58,61] Lastly, the broader features present in the FT of both BoT and EoT anodes relative to IrO_2 are consistent with a more disordered, amorphous sample environment, as evidenced by TEM.

Therefore, with the physicochemical characterization we can summarize that the surface of BoT is mainly composed by Sr and Ir, and presents very short Ir–Ir distances similar to m-$SrIrO_3$.The oxidation state of Ir in the BoT compound is close to 4+ determined from XAS. After 1000 h operation cycles the restructuration of the catalyst continues. The oxidation state of Ir on the EoT compared to BoT changed to slightly more reduced Ir. Also, the formation of sponge-like particles with voids and an amorphous surface layer of Ir–O–H is observed. SEM images reveal the agglomeration of the particles with the loss of the small ones and the big particles getting bigger. This kind of agglomeration has been previously observed in this material after 5000 OER cycles.[29] The agglomeration of this particles into larger ones can explain the large durability of the material.

3. Conclusions

In this work we have developed an anode with Sr_2CaIrO_6 catalyst having only 0.2 mg_{Ir} cm^{-2}, which is 10 times lower compare to Ir loadings of commercial CCMs. The PEMWE cell with this anode showed a performance 1.78 V at a nominal current of 2 A cm^{-2}, at 80 °C and ambient pressure, and it is kept stable for more than 1000 h. Spectroscopy studies conducted before and after 1000 h of operation in PEMWE reveal a strong reconstruction of the initial Sr_2CaIrO_6 sample. After 1000 h of reaction, and due to the fast leaching of Ca and Sr, the surface develops a sponge-type morphology conformed by small nanoregions of Ir–O–H that are responsible of the high OER performance. Most of the Ca and Sr are leached out from Sr_2CaIrO_6 but traces of them remain after the aging test. Regarding the morphology and structure of the catalyst layer itself, despite the structure is full covered of ionomer after operation, the electrochemical activity is consistently high,

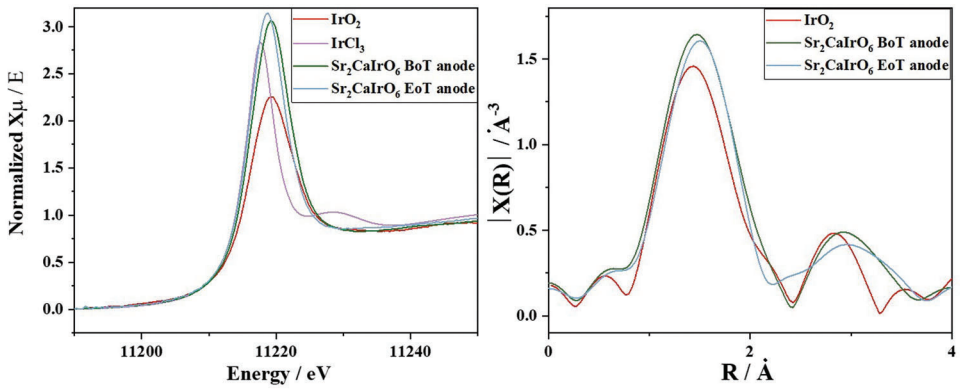

Figure 9. a) X-ray absorption near edge structure (XANES) signals of the Ir L_3-edge and b) Fourier transform extended X-ray absorption fine structure (FT-EXAFS) of BoT anode, EoT anode, Ir black, IrO_2, and $IrCl_3$ standards.

indicating that only the electronic contact to the PTL is critical, and not the in-plane conductivity of the catalyst layer. In this regard, the choice of catalyst and how connect it with the PTL (interface catalyst layer/PTL) has an outmost importance and is the key to produce catalyst layers with low Ir loadings.

The unconventional structure Sr_2CaIrO_6 also contributes to the reduction of Ir in the catalyst layer and demonstrates a new approach that can be expected to lead to further improvements and enables long-term operation without a significant decrease in catalytic activity. Anodes with low Ir loadings can be established as the new state of art in PEMWE making it more economically attractive. Our results open new perspectives for scaling low-cost PEMWE technology for large-scale production of green H_2.

4. Experimental Section

Physicochemical Characterization: The phases and crystal structure of the phases in the CCM were analyzed with a X-ray polycrystal PANalytical X´Pert PRO using nickel-filtered CuKα (1.541874 Å) radiation, with a 0.04° step size and accumulating 20 s per point.

TEM, HRTEM, and X-ray EDX were recorded in a JEOL 2100 field emission gun transmission electron microscope operating at 200 kV and equipped with an EDX Microanalysis system by Oxford INCA. The specimen was prepared by scratching catalyst from the CCM and deposited it on a Cu grid supporting a lacey carbon film.

XPS were recorded in a SPECS customized system equipped with a nonmonochromatic X-ray source XR 50 and a hemispherical energy analyzer PHOIBOS 150 using the X-ray MgK line (1253.6 eV) (operating at 200 W/12 kV). The energy regions of interest were scanned at increments of 0.1 eV and fixed pass energy of 20 eV. The pressure of the analysis chamber was maintained at 3×10^{-10} mbar. The position of the C 1s core-level peak was set at 284.6 eV. Spectra were analyzed using the XPSCasa Software. For the XAS measurements, the Ir LIII-edge data was collected in transmission and fluorescence modes at the CLÆSS beamline[62] of the ALBA synchrotron. References were prepared as pellets of powders diluted in cellulose so the data was collected in transmission; while samples of BoT and EoT anodes were run directly on the CCM, so the data were collected in fluorescence mode. Several scans were measured to ensure reproducibility and a good signal to noise ratio. The data were treated with the Demeter[63] package and the energy was calibrated to the maximum of the first inflection point of the Ir Black spectrum taken as 11215 eV.

SEM was performed with a JEOL field emission microscope (JSM-7200F) with Schottky–Emitter to observe the surface and the cross-sections of the CCLs. For surface observation samples were prepared by cutting approximately 0.5 × 0.5 cm^2 from the CCM and glued with double sided carbon tape to the SEM sample holder. For secondary electron observation the working distance was kept at 4 mm for improved resolution using lower electron detector while a working distance of 10 mm was chosen for EDX measurements as the detector is calibrated for this distance. The relevant imaging data is always shown in the legend of each SEM image. The EDX mapping of the surface and of the cut samples were performed with the attached Bruker Quantax Energy dispersive X-ray system (Quantax XFlash6/60) at 15 kV as the high voltage is needed for EDX for heavier elements. Ion cut samples were prepared using a Jeol ion cut polisher (Ion cutting system JEOL IB-19520/CCP, used with Argon gas) with 6 kV for 6 h for each sample at room temperature while swinging the sample stage during the cutting process.

AFM measurements were performed before and after the stability test measurements. In addition, a sample after activation was analyzed with AFM. The sample was cut with a razor blade and was then attached to a 12 mm steel disc with conductive double-sided tape. Conductive tape was also placed on a part of the top of the catalyst layer to ensure electrical contact. This setup was attached to the AFM with neodymium magnets. AFM measurements were performed with a Bruker ICON XR AFM (Bruker Nano Surfaces Inc., Karlsruhe, Baden-Württemberg, Germany) in either PF-QNM or PF TUNA conductive tapping mode. Conductive tapping, while averaging the current over the whole cycle (TUNA current) or over the time in contact with the sample (contact current) with a lock-in amplifier, was performed (PF-TUNA, Bruker) on the surface of the catalyst layers with PPP-NCHPt tips (Nanosensors). For higher resolution images SSS-FMR tips with a tip radius of <2 nm were used (Nanosensors).

Half-Cell Electrochemical Characterization: The electrochemical performance was recorded using an Autolab PGstat 302N potentiostat/galvanostat. A standard three-compartment glass cell was used and a RDE (Pine Research Instruments). A graphite bar was used as the counter electrode. An Ag/AgCl (3 M) electrode was used as the reference electrode. The catalyst was deposited as an ink (5 $mg_{catalyst}$, 1 mg_{vulcan}, 0.03 mL_{Nafion}, and 0.97 mL_{THF}) on a glassy carbon working electrode. The ink was prepared by mixing the oxide with carbon black (Vulcan-XC-72R) to improve the electrical conductivity. The mixture was sonicated with an Ultrasonic Processor UP50H (Hielscher). An amount of 10 µL of ink was dropped onto an electrode of 0.196 cm^2 of area, with a catalyst loading of 0.25 $mg_{catalyst}$ cm^{-2}. The Ir loading is 0.096 mg_{Ir} cm^{-2} for Sr_2CaIrO_6. The OER was assessed by recording cyclic voltammograms between 1.1 and 1.7 V_{RHE} at 10 mVs^{-1} and a rotation rate of 1600 rpm. The measurements were performed in an O_2 saturated 0.1 M $HClO_4$ electrolyte to assure the O_2/H_2O equilibrium at 1.23 V. The OER kinetic curves were capacitance-corrected by using the average of the anodic and cathodic curves and *i*R-corrected by using the formula $E - iR_{corrected} = E_{applied} - iR$, where i is the current and R is the ohmic electrolyte resistance ($R = 29\ \Omega$) obtained from EIS at open circuit voltage.

CCM Preparation and PEMWE Measurements: CCMs were prepared by the wet spraying technique using a vacuum heating table (Fuel Cell Store) to hold the Nafion 212 PEM (50 µm) substrate in place and heat it to 100 °C during deposition. The distance between spraying nozzle and substrate was kept at 6 cm, and the ink deposition rate was limited to 2–3 min mL^{-1}. The inks were prepared by mixing 1 mg of catalyst in 1 mL of ultrapure H_2O (MiliQ, 18 MΩ cm^{-1}) and the desired amount of Nafion D521 solution (5 wt% in lower aliphatic alcohols and water) to achieve an ionomer content of 25 and 30 wt% in the dry anode and cathode layer, respectively. The mixture was sonicated for at least 1 h until the catalyst was well dispersed. An amount of 1 mL of isopropanol (IPA, ACS reagent, ≥ 99.5%) was added and the mixture was sonicated for 10 min to reach the adequate dispersion and homogeneity of the ink. This process was scaled up to the desired volume of ink. After spraying and drying, the CCM was hot pressed at 5 MPa and 125 °C. The resulting loading of Ir at the anode was 0.2 mg cm^{-2} and the loading of Pt at the cathode was 0.4 mg cm^{-2}. Ca and Sr will leach out in the process of OER electrolysis and could affect strongly the PEMWE performance, likely due to Sr and Ca cations displacing protons in the ionomer and PEM. Therefore, the CCM was subjected to a protocol of activation, which involves an extensive chemical cleaning in diluted H_2SO_4 and electrochemical cycling, until the performance of the PEMWE does not change anymore. At this point the Sr and Ca on the surface of catalyst have been completely leached out posing no danger in affecting the PEMWE performance, as we later demonstrate in the durability test.

For benchmark catalyst test, CCMs with an iridium oxide anode, Pt-based cathode, and chemically stabilized Nafion 115 membrane (125 µm) were used for all electrochemical tests. The loading of the catalyst is 2 and 0.95 mg_{Pt} cm^{-2}.

The PEMWE setup optimized for long term measurements and the anode and cathode water flow rate was 2.5 L h^{-1}. On both the anode and cathode side, a Ti PSL on Ti mesh (PSL/mesh-PTL) compound PTL produced by diffusion bonding[40] coated with Pt[64] was deployed. On the cathode, a carbon paper sheet (Spectracarb 2050A-1050) was used as an additional layer contacting the cathode catalyst layer on one, and the PTL on the other side. On both the anode and cathode side Ti-BPPs were employed. The cell active area was 4 cm^2 and in both setups and tests were carried out at 80 °C and ambient pressure. The polarization curves were measured galvanostatically according to the JRC EU-harmonized procedure,[65] employing a dwell and consecutive recording period of 10 s for each current step. HFR was obtained from the high-frequency intercept of the Nyquist plot with the real axis and Tafel slopes obtained of the *i*R-free cell voltage are represented as a linear fit between 10 and 100 mA cm^{-2}.

Supporting Information

Supporting Information is available from the Wiley Online Library or from the author.

Acknowledgements

The authors acknowledge PROMET-H2 project. This project has received funding from the European Union's Horizon 2020 research and innovation programme under grant agreement No 862253. J.T. wishes to acknowledge the Deutsche Akademische Austausch Dienst (DAAD), Scholarship code number 57540124. M.R. and S.R. thank financial support from grants PID2019-103967RJ-I00 and PID2020-116712RB-C21; J.A.A. thanks support to the Project PID2021-122477OB-I0, all funded by MCIN/AEI/10.13039/501100011033. XAS experiments were performed at the BL22-CLÆSS beamline at the ALBA Synchrotron with the collaboration of ALBA staff as part of projects 2022035822 and 2022035785.

Open access funding enabled and organized by Projekt DEAL.

Conflict of Interest

The authors declare no conflict of interest.

Data Availability Statement

The data that support the findings of this study are available from the corresponding author upon reasonable request.

Keywords

degradation, iridium, low loading, OER, PEM water electrolysis

Received: December 6, 2022
Revised: March 27, 2023
Published online:

[1] IEA, *Global Energy Review 2019 – The Latest Trends in Energy and Emissions in 2019*, **2020**.
[2] Hydrogen Europe, *Clean Hydrogen Monitor 2022*, **2022**.
[3] IRENA, *Green Hydrogen Cost Reduction. Scaling up Electrolysers to Meet the 1.5 °C Climate Goal*, International Renewable Energy Agency, Abu Dhabi **2020**.
[4] European Commission, *A Hydrogen Strategy for a Climate Neutral Europe*, **2020**.
[5] *PEM Electrolysis for Hydrogen Production Principles and Applications*, 1st ed. (Eds: D. Bessarabov, H. Wang, H. Li, N. Zhao), CRC Press, Boca Raton **2015**.
[6] A. Buttler, H. Spliethoff, *Renewable Sustainable Energy Rev.* **2018**, *82*, 2440.
[7] *Multi-Annual Work Programme 2021–2027*, European Agency for Special Needs and Inclusive Education **2021**.
[8] S. Park, J. W. Lee, B. N. Popov, *Int. J. Hydrogen Energy* **2012**, *37*, 5850.
[9] M. Carmo, D. L. Fritz, J. Mergel, D. Stolten, *Int. J. Hydrogen Energy* **2013**, *38*, 4901.
[10] T. Reier, H. N. Nong, D. Teschner, R. Schlögl, P. Strasser, R. Tobias, N. H. Nhan, T. Detre, S. Robert, S. Peter, T. Reier, H. N. Nong, D. Teschner, R. Schlögl, P. Strasser, *Adv. Energy Mater.* **2017**, *7*, 1601275.
[11] D. Lebedev, M. Povia, K. Waltar, P. M. Abdala, I. E. Castelli, E. Fabbri, M. V. Blanco, A. Fedorov, C. Copéret, N. Marzari, T. J. Schmidt, *Chem. Mater.* **2017**, *29*, 5182.
[12] L. Wang, V. A. Saveleva, S. Zafeiratos, E. R. Savinova, P. Lettenmeier, P. Gazdzicki, A. S. Gago, K. A. Friedrich, *Nano Energy* **2017**, *34*, 385.
[13] H. J. Song, H. Yoon, B. Ju, D. W. D.-W. Kim, *Adv. Energy Mater.* **2021**, *11*, 1.
[14] P. Lettenmeier, L. Wang, U. Golla-Schindler, P. Gazdzicki, N. A. Cañas, M. Handl, R. Hiesgen, S. S. Hosseiny, A. S. Gago, K. A. Friedrich, *Angew. Chem., Int. Ed.* **2016**, *55*, 742.
[15] I. Katsounaros, S. Cherevko, A. R. Zeradjanin, K. J. J. J. Mayrhofer, *Angew. Chem., Int. Ed.* **2014**, *53*, 102.
[16] P. Lettenmeier, R. Wang, R. Abouatallah, S. Helmly, T. Morawietz, R. Hiesgen, S. Kolb, F. Burggraf, J. Kallo, A. S. Gago, K. A. Friedrich, *Electrochim. Acta* **2016**, *210*, 502.
[17] Johnson Matthey, PGM Market Report, Johnson Matthey, London **2021**.
[18] M. Möckl, M. F. Ernst, M. Kornherr, F. Allebrod, M. Bernt, J. Byrknes, C. Eickes, C. Gebauer, A. Moskovtseva, H. A. Gasteiger, *J. Electrochem. Soc.* **2022**, *169*, 064505.
[19] H. S. H.-S. Oh, H. N. Nong, T. Reier, M. Gliech, P. Strasser, *Chem. Sci.* **2015**, *6*, 3321.
[20] E. A. Paoli, F. Masini, R. Frydendal, D. Deiana, C. Schlaup, M. Malizia, T. W. Hansen, S. Horch, I. E. L. L. Stephens, I. Chorkendorff, *Chem. Sci.* **2015**, *6*, 190.
[21] O. Diaz-Morales, S. Raaijman, R. Kortlever, P. J. Kooyman, T. Wezendonk, J. Gascon, W. T. Fu, M. T. M. Koper, *Nat. Commun.* **2016**, *7*, 12363.

[22] S. Geiger, O. Kasian, M. Ledendecker, E. Pizzutilo, A. M. Mingers, W. T. Fu, O. Diaz-Morales, Z. Li, T. Oellers, L. Fruchter, A. Ludwig, K. J. J. Mayrhofer, M. T. M. Koper, S. Cherevko, *Nat. Catal.* **2018**, *1*, 508.
[23] X. Liang, L. Shi, Y. Liu, H. Chen, R. Si, W. Yan, Q. Zhang, G.-D. G. D. Li, L. Yang, X. Zou, *Angew. Chem., Int. Ed.* **2019**, *58*, 7631.
[24] R. Zhang, N. Dubouis, M. Ben Osman, W. Yin, M. T. Sougrati, D. A. D. Corte, D. Giaume, A. Grimaud, *Angew. Chem., Int. Ed.* **2019**, *131*, 4619.
[25] M. Bernt, A. Siebel, H. A. Gasteiger, *J. Electrochem. Soc.* **2018**, *165*, F305.
[26] M. Bernt, A. Hartig-Weiß, M. F. Tovini, H. A. El-Sayed, C. Schramm, J. Schröter, C. Gebauer, H. A. Gasteiger, *Chem. Ing. Tech.* **2020**, *92*, 31.
[27] M. A. Hubert, A. M. Patel, A. Gallo, Y. Liu, E. Valle, M. Ben-Naim, J. Sanchez, D. Sokaras, R. Sinclair, J. K. Nørskov, L. A. King, M. Bajdich, T. F. Jaramillo, *ACS Catal.* **2020**, *10*, 12182.
[28] M. Retuerto, L. Pascual, O. Piqué, P. Kayser, M. A. Salam, M. Mokhtar, J. A. Alonso, M. Peña, F. Calle-Vallejo, S. Rojas, *J. Mater. Chem. A* **2021**, *9*, 2980.
[29] M. Retuerto, L. Pascual, J. Torrero, M. A. Salam, Á. Tolosana-Moranchel, D. Gianolio, P. Ferrer, P. Kayser, V. Wilke, S. Stiber, V. Celorrio, M. Mokthar, A. S. Gago, K. A. Friedrich, M. A. Peña, J. A. Alonso, D. G. Sanchez, S. Rojas, *Nat. Commun.* **2022**, *13*, 7935.
[30] P. Kayser, M. J. Martínez-Lope, J. A. Alonso, M. Retuerto, M. Croft, A. Ignatov, M. T. Fernández-Díaz, M. J. Martínez-Lope, J. A. Alonso, M. Retuerto, M. Croft, A. Ignatov, M. T. Fernández-Díaz, *Eur. J. Inorg. Chem.* **2014**, *2014*, 178.
[31] C. C. L. L. McCrory, S. Jung, J. C. Peters, T. F. Jaramillo, *J. Am. Chem. Soc.* **2013**, *135*, 16977.
[32] L. Yang, G. Yu, X. Ai, W. Yan, H. Duan, W. Chen, X. Li, T. Wang, C. Zhang, X. Huang, J.-S. Chen, X. Zou, *Nat. Commun.* **2018**, *9*, 5236.
[33] X. Liang, L. Shi, R. Cao, G. Wan, W. Yan, H. Chen, Y. Liu, X. Zou, *Adv. Mater.* **2020**, *32*, 2001430.
[34] Z. Fan, Y. Ji, Q. Shao, S. Geng, W. Zhu, Y. Liu, F. Liao, Z. Hu, Y. C. Chang, C. W. Pao, Y. Li, Z. Kang, M. Shao, *Joule* **2021**, *5*, 3221.
[35] G. Wu, X. Zheng, P. Cui, H. Jiang, X. Wang, Y. Qu, W. Chen, Y. Lin, H. Li, X. Han, Y. Hu, P. Liu, Q. Zhang, J. Ge, Y. Yao, R. Sun, Y. Wu, L. Gu, X. Hong, Y. Li, *Nat. Commun.* **2019**, *10*, 4855.
[36] J. Zhu, Z. Chen, M. Xie, Z. Lyu, M. Chi, M. Mavrikakis, W. Jin, Y. Xia, *Angew. Chem., Int. Ed.* **2019**, *58*, 7244.
[37] G. Jiang, H. Yu, D. Yao, Y. Li, J. Chi, H. Zhang, Z. Shao, *J. Mater. Chem. A* **2022**, *10*, 11893.
[38] U. Babic, M. Suermann, F. N. Büchi, L. Gubler, T. J. Schmidt, *J. Electrochem. Soc.* **2017**, *164*, F387.
[39] K. Ayers, N. Danilovic, R. Ouimet, M. Carmo, B. Pivovar, M. Bornstein, *Annu. Rev. Chem. Biomol. Eng.* **2019**, *10*, 219.
[40] S. Stiber, H. Balzer, A. Wierhake, F. J. Wirkert, J. Roth, U. Rost, M. Brodmann, J. K. Lee, A. Bazylak, W. Waiblinger, A. S. Gago, K. A. Friedrich, *Adv. Energy Mater.* **2021**, *11*, 2100630.
[41] European Commission, PRETZEL–Novel Modular Stack Design for High Pressure PEM Water Electrolyzer Technology with Wide Operation Range and Reduced Cost, **2018**.
[42] T. L. Doan, H. E. Lee, M. Kim, W. C. Cho, H. S. Cho, T. Kim, *J. Power Sources* **2022**, *533*, 231370.
[43] G. Jiang, H. Yu, Y. Li, D. Yao, J. Chi, S. Sun, Z. Shao, *ACS Appl. Mater. Interfaces* **2021**, *13*, 15073.
[44] S. Chatterjee, X. Peng, S. Intikhab, G. Zeng, N. N. Kariuki, D. J. Myers, N. Danilovic, J. Snyder, *Adv. Energy Mater.* **2021**, *11*, 2101438.
[45] F. J. Hackemüller, E. Borgardt, O. Panchenko, M. Müller, M. Bram, *Adv. Eng. Mater.* **2019**, *21*, 1801201.
[46] K. E. Ayers, J. N. Renner, N. Danilovic, J. X. Wang, Y. Zhang, R. Maric, H. Yu, *Catal. Today* **2016**, *262*, 121.
[47] C. Rakousky, U. Reimer, K. Wippermann, S. Kuhri, M. Carmo, W. Lueke, D. Stolten, *J. Power Sources* **2017**, *342*, 38.
[48] A. Grimaud, A. Demortière, M. Saubanère, W. Dachraoui, M. Duchamp, M.-L. Doublet, J.-M. Tarascon, *Nat. Energy* **2016**, *2*, 16189.
[49] N. Li, L. Cai, C. Wang, Y. Lin, J. Huang, H. Sheng, H. Pan, W. W. Zhang, Q. Ji, H. Duan, W. Hu, W. W. Zhang, F. Hu, H. Tan, Z. Sun, B. Song, S. Jin, W. Yan, *J. Am. Chem. Soc.* **2021**, *143*, 18001.
[50] T. Morawietz, M. Handl, C. Oldani, K. A. Friedrich, R. Hiesgen, *Fuel Cells* **2018**, *18*, 239.
[51] M. Lopez-Haro, L. Guétaz, T. Printemps, A. Morin, S. Escribano, P.-H. Jouneau, P. Bayle-Guillemaud, F. Chandezon, G. Gebel, *Nat. Commun.* **2014**, *5*, 5229.
[52] T. Pawluk, L. Wang, *J. Phys. Chem. C* **2007**, *111*, 6713.
[53] C. A. Stowell, B. A. Korgel, *Nano Lett.* **2005**, *5*, 1203.
[54] I. V. Yentekakis, G. Goula, S. Kampouri, I. Betsi-Argyropoulou, P. Panagiotopoulou, M. J. Taylor, G. Kyriakou, R. M. Lambert, *Catal. Lett.* **2018**, *148*, 341.
[55] Y. Chen, H. Li, J. Wang, Y. Du, S. Xi, Y. Sun, M. Sherburne, J. W. Ager, A. C. Fisher, Z. J. Xu, *Nat. Commun.* **2019**, *10*, 572.
[56] I. Qasim, B. J. Kennedy, M. Avdeev, *J. Mater. Chem. A* **2013**, *1*, 3127.
[57] H. P. Singh, *Acta Crystallogr., Sect. A: Found. Crystallogr.* **1968**, *24*, 469.
[58] A. A. Bolzan, C. Fong, B. J. Kennedy, C. J. Howard, *Acta Crystallogr. Sect. B* **1997**, *53*, 373.
[59] L. C. Seitz, C. F. Dickens, K. Nishio, Y. Hikita, J. Montoya, A. Doyle, C. Kirk, A. Vojvodic, H. Y. Hwang, J. K. Norskov, T. F. Jaramillo, *Science (80-.).* **2016**, *353*, 1011.
[60] V. Pfeifer, T. E. Jones, J. J. Velasco Vélez, C. Massué, R. Arrigo, D. Teschner, F. Girgsdies, M. Scherzer, M. T. Greiner, J. Allan, M. Hashagen, G. Weinberg, S. Piccinin, M. Hävecker, A. Knop-Gericke, R. Schlögl, *Surf. Interface Anal.* **2016**, *48*, 261.
[61] D. Weber, L. M. Schoop, D. Wurmbrand, S. Laha, F. Podjaski, V. Duppel, K. Müller, U. Starke, B. V. Lotsch, *J. Mater. Chem. A* **2018**, *6*, 21558.
[62] L. Simonelli, C. Marini, W. Olszewski, M. Avila Perez, N. Ramanan, G. Guilera, V. Cuartero, K. Klementiev, *Cogent Phys.* **2016**, *3*, 1231987.
[63] B. Ravel, M. Newville, *J. Synchrotron Radiat.* **2005**, *12*, 537.
[64] P. Lettenmeier, R. Wang, R. Abouatallah, F. Burggraf, A. S. Gago, K. A. Friedrich, *J. Electrochem. Soc.* **2016**, *163*, F3119.
[65] T. Malkow, A. Pilenga, G. Tsotridis, *EU Harmonised Polarisation Curve Test Method for Low-Temperature Water Electrolysis*, Publications Office of the European Union, Luxembourg, **2018** https://doi.org/10.2760/179509.